TJNN Thai Journal of Nanoscience and Nanotechnology

Nanosized Natural Minerals as Sustainable Fillers for Near-Infrared Shielding Coatings: Comparative Study of Rutile, Leucoxene, Ilmenite, and Hydroilmenite

Akepawit Thanachokchaiwat[1], Thanaphon Kansaard[1], Maneerat Songpanit[1], and Weerachon Phoohinkong[2,*]

[1]*School of Integrated Innovative Technology, King Mongkut's Institute of Technology Ladkrabang, Bangkok, 10520, Thailand*
[2]*Faculty of Science and Technology, Suan Dusit University, Bangkok, 10300, Thailand*

Received: 22 November 2025, Revised: 29 December 2025, Accepted: 30 December 2025

Abstract

This study investigates nanosized Thai natural minerals rutile, leucoxene, ilmenite, and hydroilmenite as sustainable fillers for near-infrared (NIR) shielding coatings. The minerals, mainly composed of TiO_2, were processed by high-energy ball milling without chemical additives**.** The resulting natural mineral nanopowders were subsequently dispersed into a polyvinyl alcohol (PVA) matrix and applied as thin film coatings. The optical and thermal performance was found to be highly dependent on the resulting particle size and elemental composition. Specifically, the TiO_2-rich rutile and leucoxene coatings primarily enhanced IR reflection, whereas the iron-rich ilmenite and hydroilmenite coatings significantly improved NIR absorption. Critically, the ilmenite coating achieved optimal thermal performance, resulting in a maximum reduction of the model house interior temperature by 3 °C compared to the unmodified PVA film. These findings confirm the feasibility of utilizing locally sourced, processed natural minerals as cost-effective and environmentally friendly alternatives to synthetic nanomaterials, demonstrating a promising pathway for developing high-performance, energy-saving coatings.

Keywords: Near-infrared (NIR) shielding, Natural minerals, Sustainable coatings, High-energy ball milling, Nanoparticles, Thermal performance

1. Introduction

Rising global temperatures and rapid urbanization have intensified heat accumulation in buildings, leading to increased cooling energy demand, accelerated photochemical smog formation, and heightened risks to public health. Surface overheating is primarily driven by near-infrared (NIR) solar radiation, which accounts for more than half of the total heat load absorbed by building envelopes [1]-[2]. Consequently, advanced infrared (IR)-shielding materials have emerged as essential components in passive cooling technologies aimed at reducing indoor temperatures and alleviating the energy burden associated with air-conditioning systems. A wide range of IR/NIR shielding materials, including metals, transparent conductive oxides (TCOs), plasmonic NIR absorbers (e.g., CuS, Cu_2–xS) [3], polymer-based IR absorbers [4], and 2D nanomaterials, including graphene derivatives, have been developed to modulate solar heat gain [5]-[7]. However, many of these require complex synthesis, expensive precursors, or toxic solvents, limiting their scalability and sustainability. Among them, a widely studied material for optical and thermal management, titanium dioxide (TiO_2) has gained particular attention owing to its abundance, high refractive index, photostability, chemical stability, cost-efficiency, and strong light–matter interactions efficient UV and NIR responses. Its anatase and rutile polymorphs have been widely employed in coatings, smart windows, and photocatalysts, and optical coatings for thermal-management systems [8]-[11]. The optical and thermal-shielding properties of TiO_2-based materials are known to vary considerably with crystal phase, dopant concentration, and microstructural design. Anatase TiO_2 generally provides high NIR reflectance due to its wide band gap

Corresponding Author: weerachon_pho@dusit.ac.th

and relatively low absorption coefficient, whereas rutile and doped TiO_2 phases, particularly those enriched with transition metals such as Fe, are more effective NIR absorbers, owing to enhanced free-electron densities and localized electronic transitions. The introduction of F^- ions or Fe^{3+} dopants can generate Ti^{3+} species and oxygen vacancies, which facilitate localized surface plasmon resonance (LSPR) in the NIR region, thereby improving absorption efficiency [12]-[13]. Moreover, core–shell and yolk–shell nanostructures, such as Fe_2O_3@SiO_2@TiO_2 composites, have demonstrated superior NIR shielding due to their multi-phase interfaces, refractive index mismatch, and controllable light-scattering pathways. Notably, nanocomposites incorporating amorphous Fe_2O_3 coated with TiO_2 and spaced by SiO_2 interlayers exhibit improved NIR reflectance [14]. Similarly, TiO_2/$(Fe,Mn)_2O_3$ composite pigments prepared by spray pyrolysis show a significant linear increase in NIR reflectance with rising TiO_2 content, attributed to interfacial scattering, optical dilution, and phase-contrast effects. The optimized composite exhibited a total NIR reflectance of 21.0%, representing a 41% enhancement over pure $(Fe,Mn)_2O_3$, and reduced surface temperature by 6.9 °C under IR exposure [15]. These findings underscore the importance of phase composition, particle morphology, and nanostructural engineering in designing energy-saving coatings. Of particular interest to the present study is that several of these high-performance composite architectures, such as Fe_2O_3@TiO_2 and Fe_2O_3@SiO_2@TiO_2 are synergistic thermal shielding effect mechanism [16]. Therefore, Fe–Ti–Si oxide phases occur naturally in leucoxene and hydroilmenite, suggesting that thermally functional optical properties can be harnessed from low-cost, earth-abundant mineral sources without extensive chemical modification.

Nevertheless, most IR-shielding studies focus on purified or synthetically modified TiO_2 nanoparticles, which involve energy-intensive and chemically hazardous processes. In contrast, natural titanium minerals such as rutile, leucoxene, ilmenite, and hydroilmenite serve as major industrial raw materials for TiO_2 production and are available in large quantities at low cost [17]-[20]. These minerals contain intrinsic mixtures of TiO_2 and iron oxides and small impurities. These multiphase compositions can simultaneously enable IR reflectance and absorption, offering unique optical and electronic features over purified TiO_2. Despite their abundance and economic advantages, their direct use in functional thermal-shielding coatings remains largely unexplored. Most existing studies have focused on high-purity TiO_2 grades or modified Ti-based composites, which significantly increases material cost and limits large-scale implementation. Using natural minerals directly without chemical purification or a complex modification process offers a sustainable and economically attractive alternative for IR-shielding coatings. When reduced to the nanoscale, these minerals can exhibit enhanced dispersion, increased surface area, and modified optical interactions, all of which are beneficial for NIR attenuation. Despite these advantages, there is currently a lack of comparative, nanoscale studies assessing the IR-shielding behavior of different Ti-bearing natural minerals. Moreover, the structure–property relationships that govern their effectiveness as functional fillers in polymer-based NIR-shielding coatings remain poorly understood. High-energy ball milling (HEBM) is a well-established method for mineral refinement and can efficiently reduce particle size while preserving the intrinsic mineralogical features, a mechanochemical technique known to induce crystallographic disorder, reduce particle dimensions, and improve interfacial adhesion within composites. Our previous studies have demonstrated the efficacy of acid-assisted ball milling in activating ilmenite by modifying its surface characteristics, thereby improving its suitability for subsequent composite formation. Likewise, heterojunction nanocomposites synthesized from milled ilmenite and leucoxene have shown enhanced electrochemical performance due to increased surface area and favorable phase interactions [21]-[22]. To enhance the dispersion, surface activity, and particle size uniformity of the mineral ore fillers, this work therefore employs HEBM. However, the application of this technique across a broader set of Ti-rich natural minerals has not been comprehensively explored in the context of optical thermal shielding. Moreover, no prior study has simultaneously evaluated the IR-shielding performance of nanosized rutile, leucoxene, ilmenite, and hydroilmenite processed via identical milling conditions when incorporated into a polyvinyl alcohol (PVA) matrix. The mineralogical diversity among rutile, leucoxene, ilmenite, and hydroilmenite, particularly variations in TiO_2 content, Fe-oxide phases, defects, and nanostructures, influence on milling condition may strongly influence their suitability as NIR-shielding fillers. We hypothesize that the optical and thermal-shielding behaviors of nanosized natural minerals are governed by their intrinsic mineral composition and nanoscale structural features.

Specifically, minerals with higher TiO_2 content and optimized Fe-oxide components (e.g., rutile and leucoxene) are expected to show a different effect on NIR attenuation relative to ilmenite and hydroilmenite. This study investigates the NIR-shielding efficiency of nanosized Thai natural minerals rutile, leucoxene, ilmenite, and hydroilmenite incorporated into polyvinyl alcohol (PVA) coatings. By correlating their mineralogical characteristics with optical transmission and thermal-management performance, we aim to clarify the structure–property relationships governing their effectiveness as sustainable, low-cost fillers for energy-saving coatings. This work provides the first comparative analysis of these minerals at the nanoscale, highlighting their potential as locally sourced functional materials for passive cooling and building-energy-efficiency applications.

PVA is selected as the polymeric matrix in this study for its excellent film-forming ability, non-toxicity, optical clarity, and compatibility with inorganic fillers. PVA-based coatings have demonstrated high mechanical flexibility, tunable thermal stability, and ease of processing in water-based systems, which are suitable for environmentally friendly surface coatings. Furthermore, PVA supports homogeneous dispersion of nanostructured additives without the use of harmful organic solvents and can be engineered into multifunctional membranes with improved durability when combined with appropriate reinforcements [23]. Nonetheless, although the inherent hydrophilicity of PVA presents limitations for outdoor deployment, particularly under humid or rain-exposed conditions, its favorable film-forming ability, solution processability, and compatibility with a wide range of particulate fillers make it an ideal model polymer for initial investigations. In this context, PVA serves as a practical and accessible platform for evaluating the near-infrared (NIR) shielding efficacy of mineral-based nanofillers. Furthermore, its surface properties can be readily modified through hydrophobic coating techniques or chemical crosslinking, thereby improving moisture resistance. In future applications, insights gained from PVA-based composites may inform the design of more robust and durable coatings employing alternative, weather-resistant polymer matrices. Additionally, PVA-based films may still be effectively employed as interior or interlayer coatings, particularly in thermal shielding applications where direct exposure to moisture is limited [24]-[25].

2. Experimental

2.1 Materials

Natural minerals rutile, leucoxene, ilmenite, and hydroilmenite were obtained from local sources in Thailand (Sakorn Minerals Co., Ltd., Prachuap Khiri Khan Province, southern Thailand). Polyvinyl alcohol (PVA, analytical grade) was purchased from Chem-supply. All chemicals were used as received without further purification. Deionized water was used in all preparations.

Table 1. Names of the experimental conditions at constant milling time.

Natural mineral- based	400 rpm	500 rpm	600 rpm
Rutile	Ru 400 rpm	Ru 500 rpm	Ru 600 rpm
Leucoxene	Le 400 rpm	Le 500 rpm	Le 600 rpm
Ilmenite	Il 400 rpm	Il 500 rpm	Il 600 rpm
Hydroilmenite	Hy 400 rpm	Hy 500 rpm	Hy 600 rpm

Table 2. Names of the experimental conditions at constant milling speed.

Natural mineral- based	30 minutes	60 minutes	90 minutes	120 minutes
Rutile	Ru 30 min	Ru 60 min	Ru 90 min	Ru 120 min
Leucoxene	Le 30 min	Le 60 min	Le 90 min	Le 120 min
Ilmenite	Il 30 min	Il 60 min	Il 90 min	Il 120 min
Hydroilmenite	Hy 30 min	Hy 60 min	Hy 90 min	Hy 120 min

2.2 Preparation of TiO_2-Based Powders from Natural Minerals

The natural minerals (rutile, leucoxene, ilmenite, and hydroilmenite) were mechanically milled using a high-energy planetary ball mill (model: Planet M2-3F, Nagao System) equipped with zirconia milling jars and zirconia balls (3 mm diameter). The ball-to-powder mass ratio was fixed at 10:1, and no chemical additives were used during the process.

The milling procedure was carried out in two stages: Stage 1: Effect of Milling Speed: To identify the optimal rotational speed, milling was performed at 400, 500, and 600 revolutions per minute (rpm) for a fixed duration of 60 min. The extent of comminution was evaluated by comparing the particle size distributions of the milled powders. Samples were designated according to the conditions used (Table 1). Stage 2 Effect of Milling Time: Based on the results of Stage 1, the speed that yielded the smallest average particle size was selected for subsequent experiments. At this optimized speed, milling time was systematically varied at 30, 60, 90, and 120 minutes to investigate the influence of grinding duration on particle size reduction and crystallinity. The corresponding samples were designated as summarized in Table 2. After milling, all powders were collected, dried at room temperature, and stored in airtight containers to prevent contamination and moisture uptake before further characterization and coating preparation.

2.3 Characterization

The chemical compositions of the mineral samples were analyzed by X-ray fluorescence (XRF; Rigaku, ZSX PrimusI) for chemical composition determination. Crystal structures were examined by X-ray diffraction (XRD; SmartLab, Rigaku) employing Cu Kα radiation ($\lambda = 1.5406$ Å), and the average crystallite sizes were estimated using the Scherrer equation. Particle morphology was observed by scanning electron microscopy (SEM; S-8030, HITACHI). Optical transmittance and reflectance spectra across the 240–2600 nm wavelength range were measured using a UV–vis–NIR spectrophotometer (UH4150, HITACHI).

2.4 Preparation of Mineral–PVA Thin-Film Coatings

For coating preparation, a 10 wt% PVA solution was prepared by dissolving PVA in deionized water at 90 °C under continuous magnetic stirring until complete dissolution was achieved. This concentration was selected due to its optimal viscosity for film formation via the doctor-blade technique. The 10 wt% solution facilitates uniform spreading, offers adequate binding strength to prevent particle detachment, and is commonly employed as a standard formulation for comparative thermal shielding studies. After stirring for 2 h, homogeneity was confirmed by visual inspection of the suspension in a transparent container. The absence of undissolved particulates or sedimentation at the bottom of the vessel indicated complete dispersion of the PVA polymer. At this point, the milled mineral powders were added to the solution at a loading of 0.5 wt%. To aid dispersion, 0.5 wt% sodium dodecylsulfate (SDS) surfactant was added, and the suspension was stirred for an additional 10 min, subsequent loading under ultrasonicated irradiation to ensure homogeneous mixing. The resulting mixture was blade-coated onto glass substrates (2.5×3.75 cm^2) using a doctor blade with a 0.03 mm gap, a speed of 5 mm s^{-1}, and a coating length of 150 mm, and dried at room temperature.

2.5 Thermal Performance Test

The thermal shielding performance of the mineral–PVA composite films was assessed using custom-fabricated model house structures (external dimensions: 100 mm height × 135 mm width × 175 mm length; wall thickness: 10 mm), yielding an internal volume of approximately 1856.25 cm^3. The structures were fabricated from heat-resistant PETG plastic. Coated glass slides on which the mineral–PVA films were deposited were placed at the top opening of each model house to simulate incident sunlight entering through a window. All samples' assembled structures were exposed to simulated solar radiation (Philips Infrared BR125 250w E27, 1000 lux) under controlled conditions illustrated in Fig. 1. Internal air temperatures were recorded at fixed time intervals using calibrated digital thermometers (DHT22 AM2302 temperature and humidity sensor module), and results were compared against uncoated control structures to evaluate the relative thermal shielding efficacy of each film formulation.

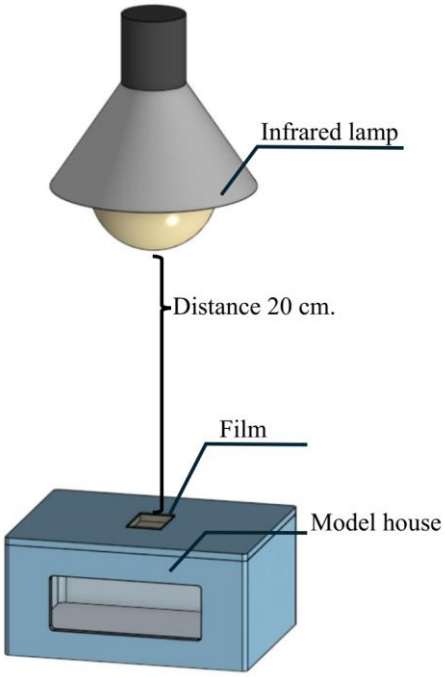

Fig. 1. Schematic illustration of the custom-fabricated model house used to evaluate the thermal shielding performance of mineral–PVA composite films.

3. Result and Discussion

3.1 Chemical Composition of Natural Minerals

Chemical composition analysis of the four natural minerals rutile, leucoxene, ilmenite, and hydroilmenite was summarized in Table 3, where titanium dioxide (TiO_2) was identified as the primary constituent, with mass percentages of 91.82%, 87.60%, 58.80%, and 67.93%, respectively. Secondary phase components for silicon dioxide (SiO_2) were presented in rutile (3.69%) and leucoxene (7.02%), while iron (III) oxide (Fe_2O_3) was found in ilmenite (26.34%) and hydroilmenite (21.99%). These secondary constituents are likely to affect material properties such as infrared reflectance and heat absorption, which are key factors for potential applications in thermal-protective coatings [1]-[2].

Table 3. Chemical composition of natural mineral-based samples.

Chemical Composition Weight %	TiO_2	Fe_2O_3	SiO_2	Al_2O_3	Cr_2O_3	ZrO_2	K_2O	MnO
Rutile	91.82	0.70	3.69	1.04	0.1	1.69	0.16	-
Leucoxene	87.60	0.92	7.02	1.80	0.33	1.15	0.28	-
Ilmenite	58.80	26.34	3.02	3.76	0.79	1.56	0.02	0.97
Hydroilmenite	67.93	21.99	1.93	1.61	1.49	0.71	0.04	0.71

3.2 Crystal Structure of Natural Minerals and Nanostructured Minerals

Figure 2 presents the X-ray diffraction (XRD) patterns of rutile mineral before and after high-energy mechanical milling at various conditions. Both the as-received rutile and all the samples milled at 400–600 rpm for 60 min, as well as at a constant speed of 600 rpm for 30–120 min, exhibit diffraction peaks corresponding to the main phase of rutile TiO_2 [JCPDS 01-078-1510], with reflections at 27.51°, 36.16°, 39.29°, 41.33°, 44.16°, 54.46°, and 56.78° assigned to the (110), (101), (200), (111), and (210), planes, respectively. Weak anatase-phase signals [JCPDS 01-070-6820] at 25.42° and 48.23° are also observed under certain conditions. No additional peaks attributable to impurity phases are detected.

Although XRF results show in Table 3 indicate that the rutile contains approximately 3.69 wt% SiO_2 before and after milling, the low concentration and poor crystallinity (likely amorphous) of SiO_2 explain the absence of distinct SiO_2 peaks in the XRD patterns [26]. A progressive decrease in the peak intensities with increasing milling speed and duration indicates a reduction in the crystallinity of TiO_2. Crystallite sizes, calculated using the Scherrer equation and summarized in Table 4, show that the initial crystallite size of as-received rutile is 40.2 nm, which is larger than that of the milled samples at 600 rpm. This observation can be attributed to the geological formation of natural rutile under prolonged high temperature and pressure, which promotes a highly ordered crystal structure [27]. With increasing milling speed and time, the crystallite size decreases to 30.87, 24.47, 22.04, and 19.51 nm at 600 rpm for 30, 60, 90, and 120 min, respectively. At lower speeds, shear forces dominate over impact forces, causing only minor disruption of the crystal lattice. This reduction in crystallite size correlates with the observed decrease in particle size [28]-[30].

The natural leucoxene and high-energy mechanically milled leucoxene revealed that corresponding to TiO_2 in the rutile phase structure with a secondary phase structure of anatase (Fig. 3). In addition, an α-SiO_2 peak [JCPDS 01-077-1060] was detected at 26.68° on the (011) plane in the unmilled leucoxene, attributable to its 7.02 % SiO_2 content, which renders the α-SiO_2 peak more distinct than in rutile. However, this α-SiO_2 peak disappeared after milling due to particle and crystallite size reduction, contribute with TiO_2 peak overlap and masking [29]. No extraneous phases were observed overall, but the TiO_2 peak intensities progressively decreased with increasing milling speed, indicating reduced crystallinity and crystallite size. The average crystallite size of TiO_2 (rutile) on the (110) plane decreased markedly from 76.55 nm in the pristine sample to 19.86 nm at the highest milling speed. Furthermore, Table 4 shows that at 600 rpm for 30–120 min, the average crystallite size decreased from 24.48 nm at 30 min to 14.24 nm at 60 min [31] before increasing to 14.63 nm and 17.66 nm at 90 and 120 min, respectively, likely due to the aggregation of small crystallites via mechanochemical reactions [28], [32]. Moreover, leucoxene contained a high proportion of TiO_2 in the rutile phase, which remains highly stable when the crystallite size exceeds ~14 nm. When sufficient energy is supplied, however, TiO_2 can transform into other phases because the surface energy of rutile is substantially higher than that of anatase [33]. Notably, when the crystallite size approached ~14 nm, slight instability of rutile occurred, promoting phase transformation or coalescence into anatase [27].

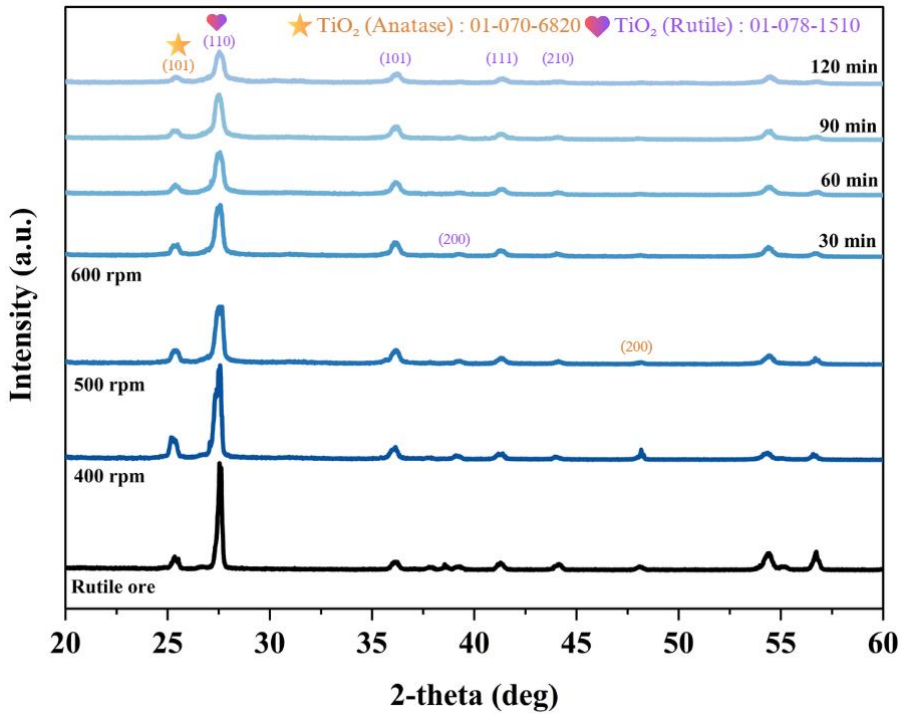

Fig. 2. X-ray diffraction patterns of rutile minerals milled at different rotational speeds and durations.

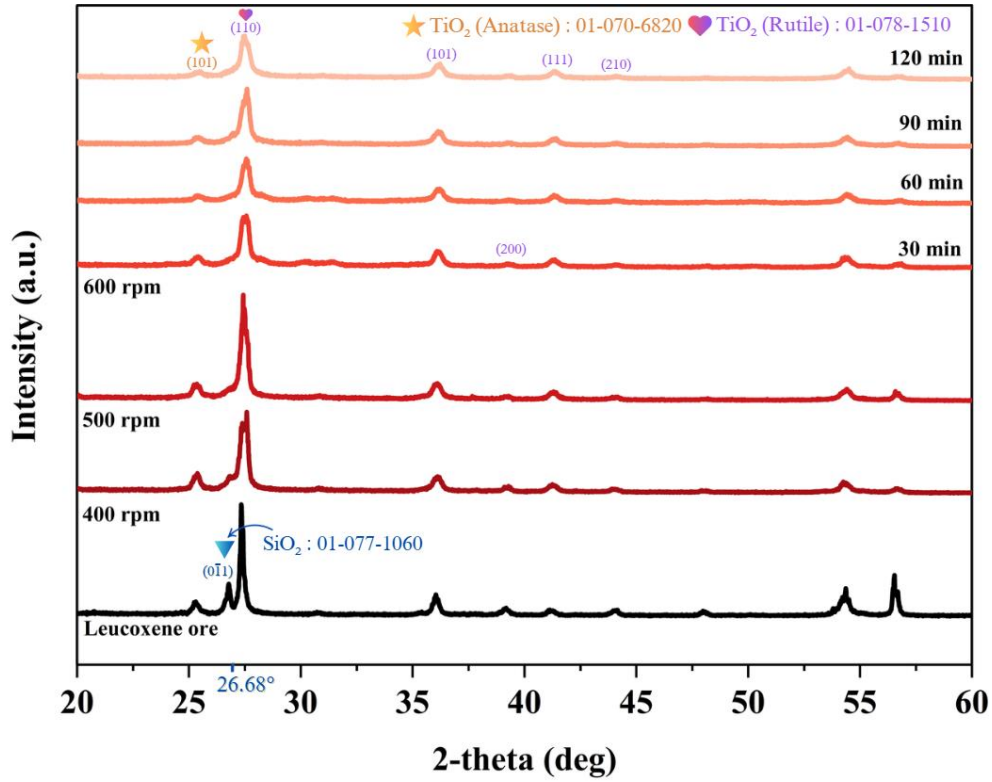

Fig. 3. X-ray diffraction patterns of leucoxene minerals milled at different rotational speeds and durations.

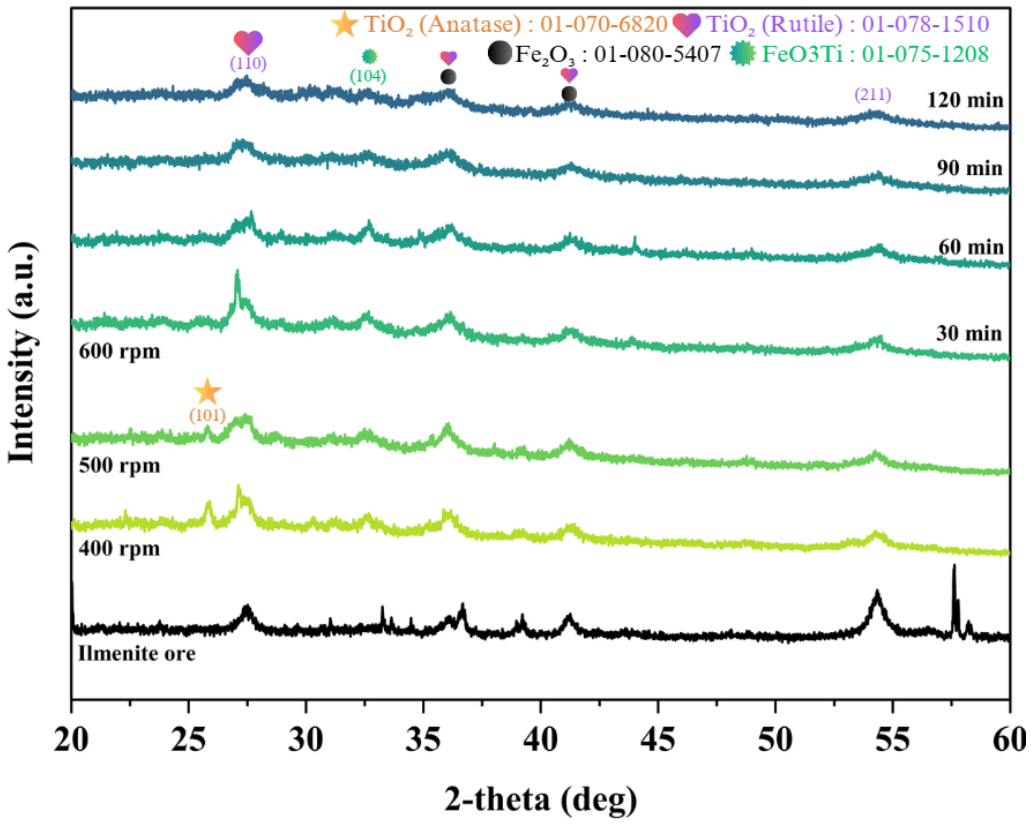

Fig. 4. X-ray diffraction patterns of ilmenite minerals milled at different rotational speeds and durations.

The natural ilmenite and mechanically milled ilmenite (Fig. 4) revealed that all unmilled and milled samples exhibited diffraction patterns consistent with TiO_2 in the rutile phase with main peaks at 27.49°, 36.03°, 41.22°, and 54.35° corresponding to the (110), (101), (111), and (211) planes, respectively. Additional peaks corresponding to Fe_2O_3 [JCPDS 01-080-5407] at 36.03° and 41.22° in the (110) and (113) planes overlapped with TiO_2 (rutile) peaks, along with $FeTiO_3$ [JCPDS 01-075-1208] at 32.51° in the (104) plane, indicating the coexistence of these phases. Milling also induced the appearance of anatase TiO_2 at 25.31°. Overall, the peak intensities varied with increasing rotation speed, reflecting crystallite size changes due to mechanochemical reactions and fragmentation from high kinetic energy, where increased shear and impact forces led to a reduction in crystallite size at higher rotation speeds [29]. As shown in Table 4, the minimum average crystallite size of 5.28 nm was obtained at 600 rpm, demonstrating the trend of decreasing particle and crystallite sizes of ilmenite prepared by high-energy mechanical milling with increasing milling duration.

The hydroilmenite minerals shown in Fig. 5 exhibited diffraction patterns consistent with the rutile TiO_2 and Fe_2O_3 phase in addition to anatase TiO_2, corresponding to the high TiO_2 content in hydroilmenite (67.93%) as determined by XRF. The crystal size also decreased significantly with increasing rotational speed, and when continuously grinding at a constant speed of 600 rpm for 30–120 min, the average crystal size slightly increased from 5.80 to 5.90 nm after 60–90 min (Table 4), which could be due to the mechanically induced crystallization from the small size of TiO_2 (rutile) crystals. However, after continuous grinding for 120 min, the average crystal size decreased to a minimum of 4.30 nm, reflecting the trend of decreasing particle size and crystallinity of hydroilmenite with grinding time. [28], [29], [32], [33]. High-energy ball milling successfully reduced the particle size of rutile, leucoxene, ilmenite, and hydroilmenite into the nanometer range without chemical additives. XRD patterns confirmed the preservation of the crystalline phases after milling, with minor broadening of peaks consistent with crystallite sizes decreased. Among the samples, rutile and leucoxene showed higher crystallinity, while ilmenite and hydroilmenite exhibited mixed oxide phases containing Ti and Fe.

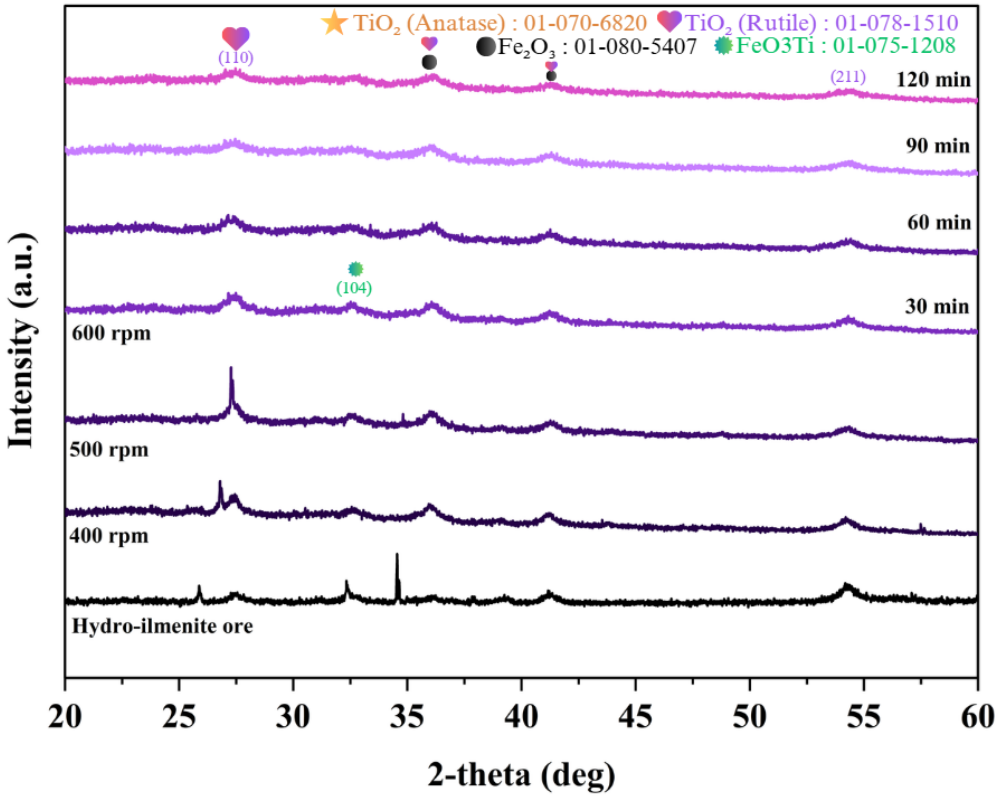

Fig. 5. X-ray diffraction patterns of hydroilmenite minerals milled at different rotational speeds and durations.

Table 4. Mean crystallite size of natural mineral-based powders before and after milling at 600 rpm for different durations.

Natural mineral-based	Mean crystal size (nm)				
	Raw mineral	30 minute	60 minute	90 minute	120 minute
Rutile	40.42	24.42	16.81	18.00	14.47
Leucoxene	63.89	24.48	14.24	14.63	17.66
Ilmenite	79.75	21.80	9.17	6.04	5.28
Hydroilmenite	89.65	6.65	5.80	5.90	4.30

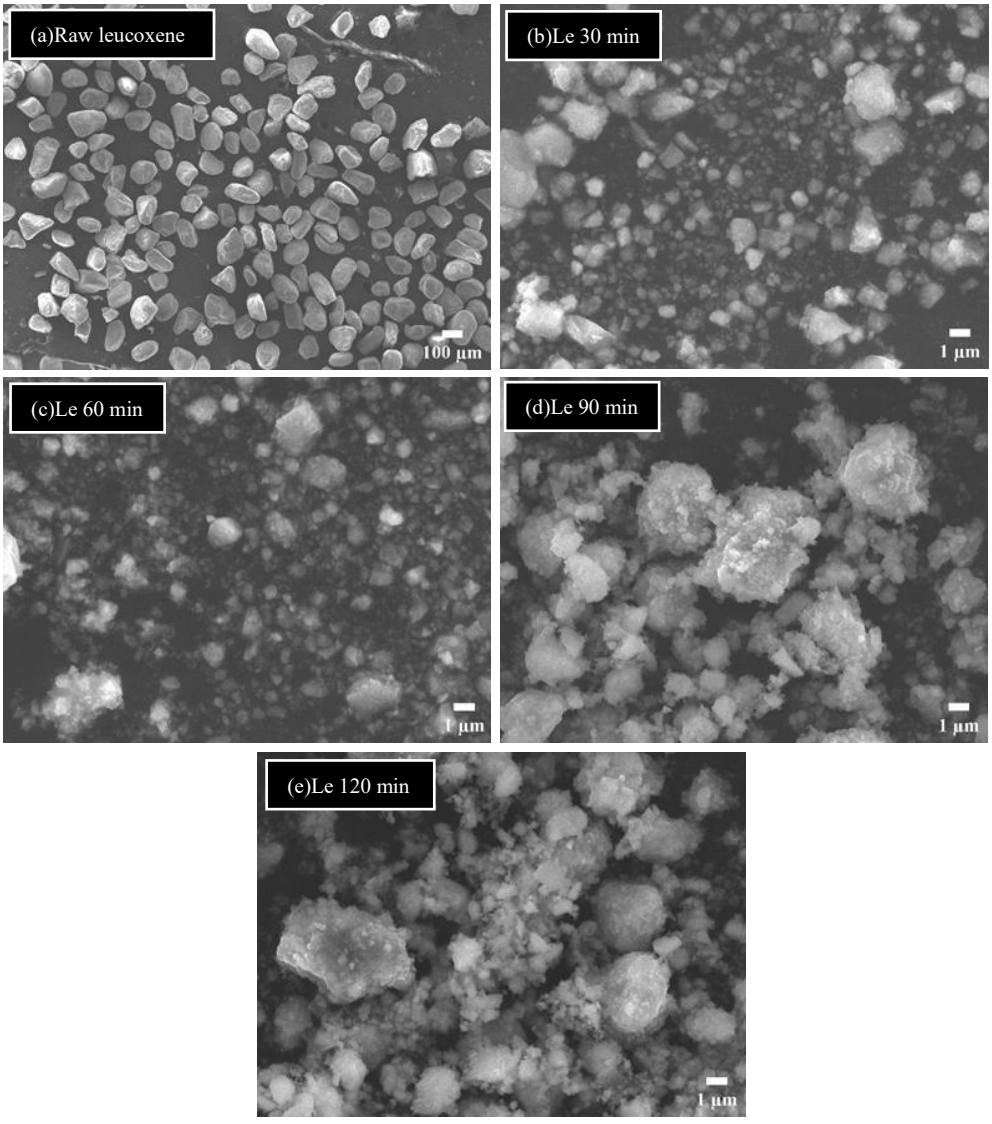

Fig. 6. SEM images of leucoxene minerals milled at 600 rpm for varying durations: (a) before milling, (b) 30 min, (c) 60 min, (d) 90 min, (e) 120 min.

3.3 Morphology of Milled Natural Mineral Powders

SEM images (Fig. 6) show that the morphological characteristics of leucoxene before and after high-energy mechanical milling, minerals consist of irregular micron-sized particles with partial agglomeration, which is a typical characteristic of mechanically milled oxide powders. After milling at

600 rpm (Fig. 6b–e), the powders exhibited more uniform nanosized particles (<100 nm). However, extending the milling time to 90–120 min led to particle agglomeration due to mechanochemical reactions [33], resulting in particle sizes larger than those observed at 30 min. This behavior corresponds to the crystallite size evolution of leucoxene observed by X-ray diffraction analysis. Particle refinement is expected to enhance dispersion in PVA coatings and improve optical interactions.

3.4 Optical and NIR Shielding Properties of Natural Mineral

Based on the chemical composition of natural minerals, two subgroups can be distinguished according to their secondary components, which influence thermal radiation shielding properties, such as absorption and reflection. The reflectivity of natural TiO_2-based minerals, rutile, leucoxene, ilmenite, and hydroilmenite, after high-energy mechanical milling at different rotational speeds of 400, 500, and 600 rpm, is presented in Fig. 7. The reflectivity trends can be classified into two characteristic groups. The first group, comprising (a) rutile and (b) leucoxene, exhibited an increase in reflectivity with increasing rotational speed. Mechanical milling reduced the particle size, producing smaller TiO_2- and SiO_2-rich components with a larger surface area, thereby altering their reflectance spectra. Leucoxene demonstrated approximately 4% higher reflectivity in the near-infrared region (800–1500 nm) compared with rutile, attributable to its higher SiO_2 content, which may enhance solar thermal radiation reflectance [2]. The second group, consisting of (c) ilmenite and (d) hydroilmenite, showed a decrease in reflectivity with increasing milling speed, suggesting enhanced absorption properties. This behavior can be explained by their relatively lower TiO_2 and higher Fe_2O_3 content, with Fe_2O_3 contributing strongly to solar thermal radiation absorption. Furthermore, both minerals originally exhibited a black, glossy, sandy appearance, but milling reduced particle size and diminished the inherent gloss, increasing surface area and resulting in lower reflectance. These findings suggest that ilmenite and hydroilmenite may serve as effective natural mineral components for coatings designed to enhance solar radiation absorption in heat-protective applications.

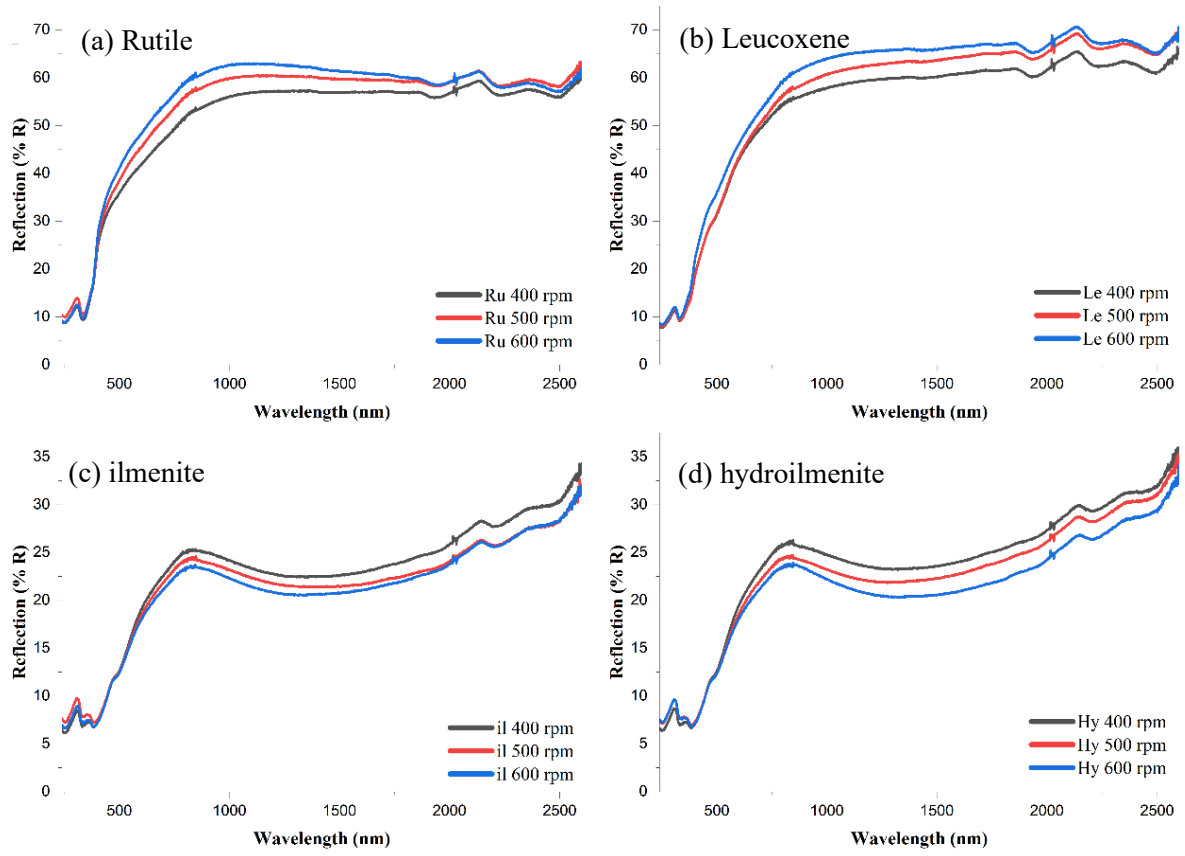

Fig. 7. UV–Vis–NIR reflectance spectra of mineral powders milled at 400–600 rpm for 60 min: (a) rutile, (b) leucoxene, (c) ilmenite, (d) hydroilmenite.

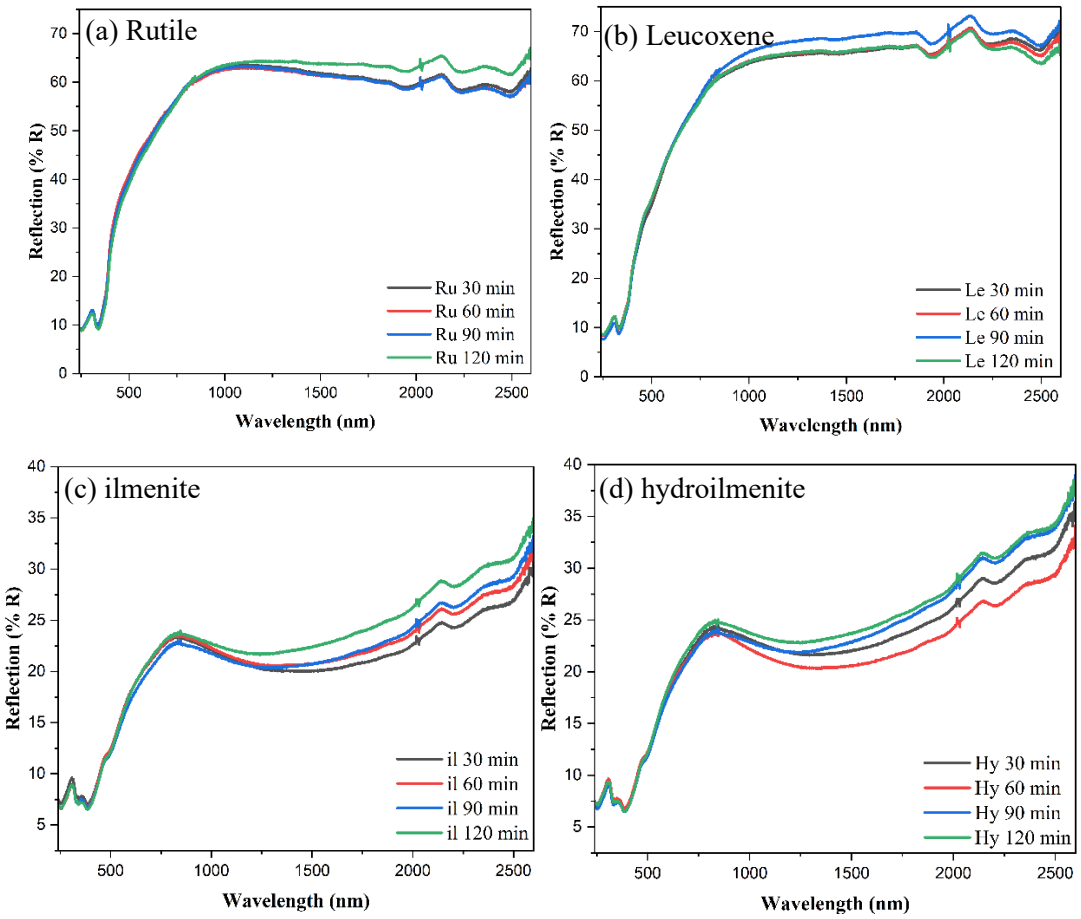

Fig. 8. UV–Vis–NIR reflectance spectra of mineral powders milled at 600 rpm for 30–120 min: (a) rutile, (b) leucoxene, (c) ilmenite, (d) hydroilmenite.

The effect of milling time on reflectance properties of TiO_2-rich minerals was examined for 30, 60, 90, and 120 minutes (Fig. 8). In the 240–800 nm range (UV to visible light), both rutile and leucoxene minerals exhibited similar reflectance spectra characteristics of their chemical structures and composition. The milled rutile for 120 minutes and leucoxene milled for 90 minutes exhibited the highest reflectance, which may be attributable to the smallest particle size in an optimal range for light scattering, thereby improving reflectance efficiency. The reflectance spectra of ilmenite and hydroilmenite exhibited a continuous increase in near-infrared reflectance with increasing milling time, which can be ascribed to size reduction of the primary TiO_2 and secondary Fe_2O_3 phases, influencing their optical response. TiO_2 inherently reflects thermal radiation due to its physical properties, while Fe_2O_3 reflects only partially and strongly absorbs in the lower infrared range owing to its bandgap characteristics. Compared with rutile and leucoxene, ilmenite and hydroilmenite displayed markedly lower reflectance, reflecting their higher absorption capability, particularly due to Fe_2O_3 content, which effectively absorbs solar thermal radiation. These findings highlight the potential of all four minerals, ilmenite, hydroilmenite, rutile, and leucoxene, as candidate materials for thermal radiation shielding, particularly when incorporated into polymer matrices such as polyvinyl alcohol to develop advanced heat-protective coatings.

The UV–Vis–NIR spectra show distinct optical behaviors depending on mineral type demonstrated that phase composition and structure strongly influence optical properties behavior. Rutile and leucoxene primarily enhanced reflectance in the NIR region (780–2500 nm), consistent with their high TiO_2 content, refractive index and strong light-scattering ability. In contrast, ilmenite and hydroilmenite exhibited stronger NIR absorption due to the presence of Fe_2O_3, which acts as an efficient absorber attributed to the Fe^{2+}/Fe^{3+} ions, which introduce additional electronic transitions. The finer powders (600 rpm) showed enhanced reflection or absorption compared with coarser powders. This

indicates that nanosizing improves optical performance by increasing surface area and light–particle interactions.

3.5 Optical Properties of Mineral–PVA Coatings

The optical performance of the mineral–PVA composite coatings was systematically investigated to assess their capability in mitigating heat transfer. quantitatively assessed by measuring the steady-state interior temperature of a model house apparatus under simulated solar irradiation. To ensure optimal performance for comparison, all mineral samples, rutile, leucoxene, ilmenite, and hydroilmenite, were prepared using the smallest particle size milling condition, which was previously determined to provide the highest near-infrared (NIR) reflectance. These milled mineral powders were uniformly dispersed within a PVA matrix and applied as thin film coatings. The results presented in Fig. 9, indicate a notable variation in thermal performance depending on the mineral filler and demonstrate a significant impact of mineral coatings on thermal management. The uncoated control film served as the baseline, recording a maximum steady-state interior temperature of 43.3°C. The application of milled mineral-PVA coatings consistently resulted in a reduction of the interior temperature. The coatings containing rutile, leucoxene, ilmenite, and hydroilmenite reduced the temperature to 42.2°C, 42.8°C, 40.3°C, and 42.9°C, respectively. The ilmenite–PVA coating demonstrated the greatest thermal efficacy, achieving a temperature reduction of 3°C compared to the uncoated control. This 3 °C surface temperature reduction represents a significant threshold for practical energy-saving applications in building envelopes. Extensive literature has established quantitative relationships between surface temperature reductions and HVAC energy consumption, demonstrating that a 1 °C decrease in surface temperature corresponds to an 8–12% reduction in HVAC energy consumption, while a 2 °C decrease may yield savings of 15–25% depending on climate and building type [34]-[35]. Thus, the 3 °C reduction observed for ilmenite–PVA coatings translates to a potential energy savings of 20–40% depending on specific building configurations and environmental conditions. These minerals, rich in Fe_2O_3 content, exhibit strong NIR absorption activity, which directly reduces the amount of heat transmitted through the film. Spectroscopic analysis (Fig. 8) provides insight into the underlying optical mechanisms. Among the mineral fillers, ilmenite and hydroilmenite exhibited the strongest NIR absorption across the 800–2500 nm range, attributable to their high Fe_2O_3 contents (>45 wt%). By contrast, rutile with negligible Fe content (~2 wt%) displayed minimal absorption. Leucoxene, with intermediate iron content, showed moderate absorption. These results suggest a direct correlation between Fe_2O_3 concentration and NIR absorbance under controlled dispersion conditions. The enhanced absorption can be attributed to the presence of Fe^{3+} ions in the hematite (α-Fe_2O_3) phase, which promote d–d electronic transitions and strong ligand field effects. Furthermore, Fe_2O_3–TiO_2 interfacial interactions are known to increase free carrier generation, facilitating plasmonic absorption within the NIR region, contributing to broadband absorption and partial reflection in the NIR range, and the TiO_2 phase exhibited NIR reflectivity. Such mechanisms are supported by several studies: Lee, Jung [14] demonstrated that nanostructured Fe_2O_3/TiO_2 composites enhanced NIR reflectance via interfacial energy modulation. Similarly, Sadeghi-Niaraki, Ghasemi [16] reported that reddish-brown Fe_2O_3@SiO_2@TiO_2 core–shell nanostructures maintained both visible coloration and high NIR reflectance. Furthermore, Hwang and Jung [15] confirmed that TiO_2/$(Fe,Mn)_2O_3$ composites display enhanced NIR reflectance attributable to synergistic absorption–scattering effects from multivalent iron oxides embedded in a dielectric matrix. While certain core–shell or composite configurations favor NIR reflection, the literature consistently affirms that Fe_2O_3 contributes substantially to NIR shielding via absorption-dominated mechanisms and/or through enhanced reflectance, depending on its phase structure, dispersion state, and composite architecture. In the present study, an absorption-dominant behavior is most plausible, considering the high Fe_2O_3 content and the intrinsically dark coloration of the ilmenite-based minerals. These findings underscore the potential of Fe_2O_3-rich minerals as viable and sustainable constituents in the design of passive NIR-shielding coatings. Conversely, TiO_2-rich minerals such as rutile and leucoxene are expected to rely primarily on IR/NIR reflection as their principal shielding mechanism. This interpretation is substantiated by experimental and theoretical observations. Spectroscopic data show that rutile- and leucoxene-based coatings exhibited the lowest NIR absorbance among all samples (Fig. 8), despite maintaining moderate surface temperature reduction in thermal performance tests. This indicates that heat mitigation in these samples is governed by optical reflection rather than absorption. Rutile TiO_2 is well-documented for its high refractive index ($n \approx 2.6$–

2.9 in the NIR region) and low extinction coefficient, both of which facilitate efficient broadband reflection and multiple light scattering [36]-[37]. These properties have been exploited in various architectures: for instance, cotton fabrics coated with rutile TiO_2 exhibited increased NIR reflectivity and reduced thermal loading under solar exposure [38]. Similarly, TiO_2-based radiative cooling films have shown strong solar reflectivity and NIR backscattering, with performance strongly influenced by particle size and phase composition [39]. Theoretical modelling has further confirmed that TiO_2 retains a high refractive index even at nanoscale dimensions, preserving its capacity for broadband NIR scattering [40]. Additionally, multiple scattering from densely packed rutile structure in the submicron regime particles can significantly enhance reflectance, especially within the NIR range [41]. Among all minerals tested, ilmenite appears to strike the most favorable balance between reflectance (contributed by TiO_2 content) and absorption (associated with Fe_2O_3 content), thereby delivering superior thermal shielding through a dual-mechanism pathway. The diagram presented in Fig. 10 conceptually illustrates the primary optical mechanisms to govern near-infrared (NIR) shielding performance in natural mineral-based coatings. The overall thermal shielding efficiency results from a synergistic interplay of these mechanisms, modulated by the mineral phase composition, particle morphology, and dispersion quality within the PVA matrix.

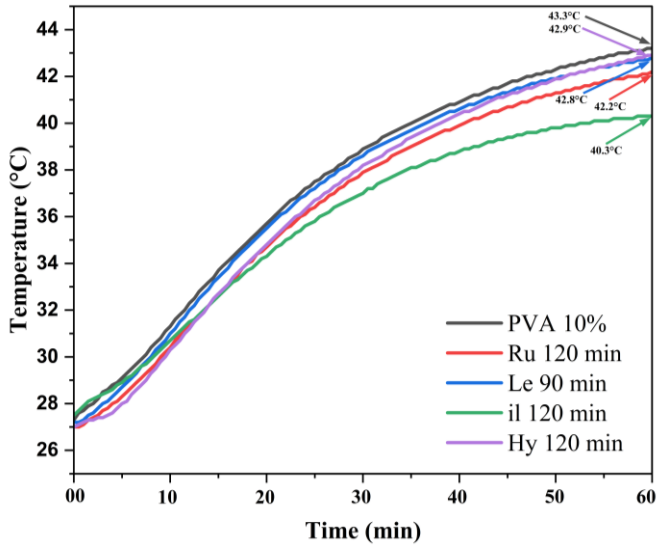

Fig. 9. Internal temperature profiles of model houses coated with PVA films containing rutile, leucoxene, ilmenite, and hydroilmenite.

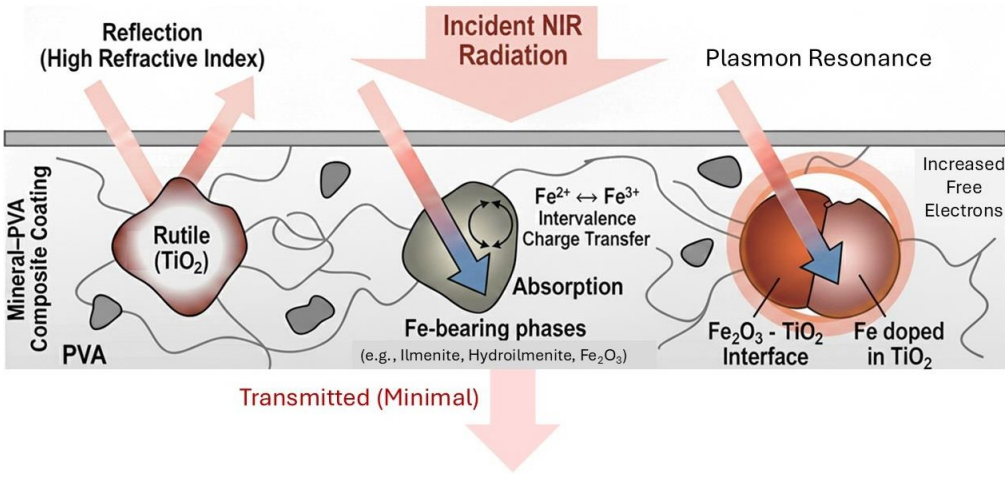

Fig. 10. Schematic illustration of the optical pathways contributing to near-infrared (NIR) shielding in mineral–PVA composite coatings.

4. Conclusion

This study successfully investigated the preparation and application of nanosized natural minerals derived from rutile, leucoxene, ilmenite, and hydroilmenite as sustainable functional fillers for near-infrared (NIR) shielding coatings. Utilizing a high-energy mechanical milling (HEMM) process, these minerals were size reduced without the use of chemical reagents and subsequently incorporated into polyvinyl alcohol (PVA) matrices to enhance the infrared (IR) blocking capabilities of the resulting coatings. The comprehensive analysis of milling parameters demonstrated that the milling speed significantly influenced the resultant mineral properties. Milling at 200–600 rpm for a fixed duration (60 minutes) showed that increasing the speed effectively reduced both crystallite and particle sizes. This size reduction directly improved the IR reflectance for the TiO_2-rich minerals (rutile and leucoxene) and enhanced the heat absorption capacity for the Fe_2O_3-containing minerals (ilmenite and hydroilmenite). Further optimization at the superior speed of 600 rpm with varied milling times (30–120 minutes) confirmed continued particle size refinement for rutile, ilmenite, and hydroilmenite. However, leucoxene displayed a tendency toward agglomeration when milled for periods exceeding 60 minutes. The performance evaluation of the final PVA-mineral coatings revealed distinct mechanisms of heat mitigation based on the mineral composition. Rutile and Leucoxene primarily function via a heat reflection mechanism. Ilmenite and Hydroilmenite primarily operate via a heat absorption mechanism. Most notably, the ilmenite sample, optimized by milling at 600 rpm for 120 minutes, yielded the most significant thermal protection, reducing the interior temperature of the model house by a maximum of 3.0°C when compared to the unmodified PVA control film. These findings conclusively affirm that the control of ball-milling parameters directly governs the resulting particle size, crystalline size, optical behavior, and ultimately the IR-shielding performance of the natural mineral-based coatings. This research validates the potential of nanosized Thai natural minerals as cost-effective and environmentally friendly alternatives to synthetic nanomaterials, establishing them as highly promising sustainable fillers for advanced, energy-saving NIR-shielding coatings.

Acknowledgments

Authors would like to thank Advanced Technology Testing and Analysis Center (ATTAC) of School of Integrated Innovative Technology (SIITec), King Mongkut's Institute of Technology Ladkrabang (KMITL) and Kyoto university under Japan-Asian Science Technology and Innovation Platform (JASTIP) program for supporting instrument and characterization facilities.

References

[1] Roy, A., Ghosh, A., Mallick, T. K., Tahir, A. A., & Sundaram, S. (2022). Smart glazing thermal comfort improvement through near-infrared shielding paraffin incorporated SnO_2-Al_2O_3 composite. *Construction and Building Materials*, *331*, 127319. DOI: 10.1016/j.conbuildmat.2022.127319.

[2] Soranakom, M. P. (2021). *Development of Fe_2O_3@SiO_2 and Fe_2O_3@$ZrSiO_4$ core-shell NIR-reflective red pigments* [Master's thesis]. King Mongkut's Institute of Technology Ladkrabang.

[3] Ng, Z. Q. C., Manzhos, S., & Sonar, P. (2020). Energy-efficient stacks—Covellite (CuS) on polyethylene terephthalate film: A sustainable solution to heat management. *The Journal of Physical Chemistry C*, *124*(5), 3314–3321. DOI: 10.1021/acs.jpcc.9b11099.

[4] Früh, A., Suseendran, D., Elmas, S., & Heitz, T. (2022). Orientation analysis of polymer thin films on metal surfaces via IR absorbance of the relative transition dipole moments. *Applied Surface Science*, *594*, 153476. DOI: 10.1016/j.apsusc.2022.153476.

[5] Liu, Q., Hao, B., Zhang, L., Wang, Y., & Zhao, Y. (2021). Ultrathin, biomimetic multifunctional leaf-like silver nanowires/$Ti_3C_2T_x$ MXene/cellulose nanofibrils nanocomposite film for high-performance electromagnetic interference shielding and thermal management. *Journal of Alloys and Compounds*, *860*, 158151. DOI: 10.1016/j.jallcom.2020.158151.

[6] Nematpour, A., Shishkin, I. I., Aliev, K. B., & Sreejith, S. (2021). Experimental mid-infrared absorption (84%) of single-layer graphene in a reflective asymmetric Fabry–Perot filter: Implications for photodetectors. *ACS Applied Nano Materials*, *4*(2), 1495–1502. DOI: 10.1021/acsanm.0c03036.

[7] Wang, Y., Zhang, X., Li, J., & Zhang, Y. (2025). Recent advances in graphene-based materials for radar and infrared stealth application. *Composites Part A: Applied Science and Manufacturing*, *192*, 108807. DOI: 10.1016/j.compositesa.2024.108807.
[8] Gao, C., Li, S., Wang, J., & Zhang, H. (2024). Low infrared emissivity and corrosion resistance of TiO_2 films prepared by thermal oxidation of sputtered Ti films. *Materials Today Communications*, *41*, 111100. DOI: 10.1016/j.mtcomm.2024.111100.
[9] Hazra, S., Mallick, T. K., & Sundaram, S. (2024). Cost-efficient Ag/Ag-TiO_2 coating-based flexible transparent heat reflector for energy-saving smart windows. *ACS Applied Energy Materials*, *7*(17), 7316–7324. DOI: 10.1021/acsaem.4c01016.
[10] Singh, S., Maurya, I. C., Senapati, S., Srivastava, P., & Bahadur, L. (2017). Fabrication of highly efficient TiO_2/Ag/TiO_2 multilayer transparent conducting electrode with N ion implantation for optoelectronic applications. *Ceramics International*, *43*(13), 9759–9768. DOI: 10.1016/j.ceramint.2017.04.144.
[11] Dalapati, G. K., Sharma, H., Guchhait, A., & Chakraborty, S. (2016). Color tunable low cost transparent heat reflector using copper and titanium oxide for energy saving application. *Scientific Reports*, *6*(1), 20182. DOI: 10.1038/srep20182.
[12] Wang, D., Wu, X., & Gao, Q. (2021). Novel energy-saving window coating based on F doped TiO_2 nanocrystals with enhanced NIR shielding performance. *Ceramics International*, *47*(20), 28557–28565. DOI: 10.1016/j.ceramint.2021.07.015.
[13] Gao, Q., Wu, X., & Zhou, C. (2025). Enhancing the NIR blockage efficiency of heavily doped TiO_2 via local surface plasmon resonance modulation for energy-saving window. *Journal of Alloys and Compounds*, *1010*, 177567. DOI: 10.1016/j.jallcom.2024.177567.
[14] Lee, H. J., Jung, K. Y., & Kim, Y. S. (2021). Nanostructured Fe_2O_3/TiO_2 composite particles with enhanced NIR reflectance for application to LiDAR detectable cool pigments. *RSC Advances*, *11*(28), 16834–16840. DOI: 10.1039/D1RA02244G.
[15] Hwang, J. S., & Jung, K. Y. (2026). Enhanced near-infrared reflectance of TiO_2/$(Fe,Mn)_2O_3$ composite black pigments synthesized by spray pyrolysis. *Ceramics International*, *52*(1), 1041–1049. DOI: 10.1016/j.ceramint.2025.10.045.
[16] Sadeghi-Niaraki, S., Jafari, H., & Kiani, M. S. (2020). Cool and photocatalytic reddish-brown nanostructured Fe_2O_3@SiO_2@TiO_2 pigments. *Materials Science and Engineering: B*, *262*, 114752. DOI: 10.1016/j.mseb.2020.114752.
[17] Tahooni Bonab, S., Abdollahi, H., & Abbaspour, A. (2025). The hydrometallurgical approach in the production of a high content of titanium dioxide (TiO_2) from ilmenite, direct hydrochloric and sulfuric acid leaching and pre-treatment methods: A review. *Mineral Processing and Extractive Metallurgy Review*, *46*(4), 537–553. DOI: 10.1080/08827508.2023.2281541.
[18] Sampath, A. H. J., Premaratne, K., & Rathnayaka, S. (2023). Methods of extracting TiO_2 and other related compounds from ilmenite. *Minerals*, *13*(5), 662. DOI: 10.3390/min13050662.
[19] Noman, M. T., Ashraf, M. A., & Ali, A. (2019). Synthesis and applications of nano-TiO_2: A review. *Environmental Science and Pollution Research*, *26*(4), 3262–3291. DOI: 10.1007/s11356-018-3884-y.
[20] Fauzi, A., Santosa, S. J., & Siswanta, D. (2024). Exploring heterogenous TiO_2 nanocrystals from natural ilmenite mineral extraction for energy application. *Materials Science for Energy Technologies*, *7*, 216–227. DOI: 10.1016/j.mset.2024.01.002.
[21] Phoohinkong, W., Sirivipa, S., & Prommalikit, M. C. (2017). Electrochemical properties of nanopowders derived from ilmenite and leucoxene natural minerals. *Ceramics International*, *43*, S717–S722. DOI: 10.1016/j.ceramint.2017.02.045.
[22] Phoohinkong, W., Sirivipa, S., & Prommalikit, M. C. (2018). Synthesis of low-cost titanium dioxide-based heterojunction nanocomposite from natural ilmenite and leucoxene for electrochemical energy storage application. *Current Applied Physics*, *18*, S44–S54. DOI: 10.1016/j.cap.2017.11.006.
[23] Wei, Y., Wang, X., & Zhang, L. (2025). Polymers with tunable rigidity enable thermal stiffening peptide hydrogels and ultra-tough polyvinyl alcohol membranes. *Small*, *21*(45), e08045. DOI: 10.1002/smll.202408045.

[24] Jinsi, C. P., Sreeraj, K. P., & Jose, G. (2025). Transparent heat reflecting PVA/Cu/PVA photonic structures for energy saving smart windows. *Materials Chemistry and Physics*, *336*, 130545. DOI: 10.1016/j.matchemphys.2024.130545.
[25] Li, Y., Pu, J., & Lu, L. (2025). A quantitative analysis for radiative cooling of a novel window composed of nanoparticles film in hot seasonal region. *Applied Thermal Engineering*, *279*, 127946. DOI: 10.1016/j.applthermaleng.2024.127946.
[26] Devine, R. A. (2012). *The physics and technology of amorphous SiO_2*. Springer Science & Business Media.
[27] Meinhold, G. (2010). Rutile and its applications in earth sciences. *Earth-Science Reviews*, *102*(1), 1–28. DOI: 10.1016/j.earscirev.2010.06.001.
[28] Prommalikit, M. C. (2018). *Size reduction of ZnO powder by high energy mechanical milling process* [Master's thesis]. King Mongkut's Institute of Technology Ladkrabang.
[29] Almquist, C. B., & Biswas, P. (2002). Role of synthesis method and particle size of nanostructured TiO_2 on its photoactivity. *Journal of Catalysis*, *212*(2), 145–156. DOI: 10.1006/jcat.2002.3783.
[30] Phoohinkong, W., Sirivipa, S., & Prommalikit, M. C. (2017). Characterization and x-ray absorption spectroscopy of ilmenite nanoparticles derived from natural ilmenite ore via acid-assisted mechanical ball-milling process. *Advances in Natural Sciences: Nanoscience and Nanotechnology*, *8*(3), 035012. DOI: 10.1088/2043-6254/aa78b8.
[31] Pronpugdewatana, M. A. (2018). *Preparation of new photocatalyst from magnetic leucoxene minerals via high-energy ball milling method* [Master's thesis]. King Mongkut's Institute of Technology Ladkrabang.
[32] Baláž, P., Achimovičová, M., Baláž, M., Billik, P., Cherkezova-Zheleva, Z., Criado, J. M., Delogu, F., Dutková, E., Gaffet, E., Gotor, F. J., Kumar, R., Mitov, I., Rojac, T., Senna, M., Streletskii, A., & Wieczorek-Ciurowa, K. (2013). Hallmarks of mechanochemistry: From nanoparticles to technology. *Chemical Society Reviews*, *42*(18), 7571–7637. DOI: 10.1039/C3CS35031K.
[33] Sepelak, V., Begin-Colin, S., & Caër, G. (2012). Transformations in oxides induced by high-energy ball-milling. *Dalton Transactions*, *41*, 11927–11948. DOI: 10.1039/C2DT31403F.
[34] Rawat, M., & Singh, R. N. (2022). A study on the comparative review of cool roof thermal performance in various regions. *Energy and Built Environment*, *3*(3), 327–347. DOI: 10.1016/j.enbenv.2021.03.001.
[35] Rosado, P. J., Levinson, R., & Akbari, H. (2014). Measured temperature reductions and energy savings from a cool tile roof on a central California home. *Energy and Buildings*, *80*, 57–71. DOI: 10.1016/j.enbuild.2014.05.011.
[36] Kim, H. J., Kim, S. H., & Kim, J. H. (2020). Shape control of rutile TiO_2 particles templated using graft copolymers for thermo-shielding materials. *Ceramics International*, *46*(1), 1227–1231. DOI: 10.1016/j.ceramint.2019.09.081.
[37] Xia, Z., Wang, Y., & Chen, X. (2025). Passive radiative cooling films doped with SiO_2-TiO_2 of different particle sizes with excellent solar reflectivity and high infrared emissivity. *Solar Energy Materials and Solar Cells*, *292*, 113812. DOI: 10.1016/j.solmat.2024.113812.
[38] Wong, A., Daoud, W. A., & Liang, H. (2015). Application of rutile and anatase onto cotton fabric and their effect on the NIR reflection/surface temperature of the fabric. *Solar Energy Materials and Solar Cells*, *134*, 425–437. DOI: 10.1016/j.solmat.2014.12.025.
[39] Mishra, B. R., Sundaram, S., & Sasihithlu, K. (2024). Cooling performance of TiO_2-based radiative cooling coating in tropical conditions. *ACS Omega*, *9*(50), 49494–49502. DOI: 10.1021/acsomega.4c06208.
[40] Jalava, J. P., Paronen, M. P., & Sun, Z. (2015). Modeling TiO_2's refractive index function from bulk to nanoparticles. *Journal of Quantitative Spectroscopy and Radiative Transfer*, *167*, 105–118. DOI: 10.1016/j.jqsrt.2015.08.010.
[41] McNeil, L. E., & French, R. H. (2000). Multiple scattering from rutile TiO_2 particles. *Acta Materialia*, *48*(18), 4571–4576. DOI: 10.1016/S1359-6454(00)00243-3.